Colossal electric field control of magnetic anisotropy at ferromagnetic interfaces induced by iridium overlayer

Sohee Kwon, Phuong-Vu Ong, Qilong Sun, Farzad Mahfouzi, Xiang Li, Kang L. Wang, Y. Kato, H. Yoda, Pedram Khalili Amiri, and Nicholas Kioussis

Colossal Electric Field Control of Magnetic Anisotropy at Ferromagnetic Interfaces Induced by Iridium Overlayer

Sohee Kwon,[1, *] Phuong-Vu Ong,[1] Qilong Sun,[1] Farzad Mahfouzi,[1] Xiang Li,[2] Kang L. Wang,[2] Y. Kato,[3] H. Yoda,[3] Pedram Khalili Amiri,[4] and Nicholas Kioussis[1, †]

[1]*Department of Physics and Astronomy, California State University, Northridge, CA 91330-8268, USA*
[2]*Department of Electrical and Computer Engineering,*
University of California, Los Angeles, Los Angeles, CA 90095-1594, USA
[3]*Corporate R&D Center, Toshiba Corporation, Kawasaki 212-8582, Japan*
[4]*Electrical Engineering and Computer Science, Northwestern University, Evanston, IL 60208-3109, USA*
(Dated: February 13, 2019)

Voltage-induced magnetization switching can lead to a new paradigm enabling ultralow-power and high density instant-on nonvolatile magnetoelectric random access memory (MeRAM) devices. Two major challenges for future MeRAM devices are to achieve large perpendicular magnetic anisotropy (PMA) and high voltage-controlled magnetic anisotropy (VCMA) coefficient of heavy-metal/ferromagnet/insulator heterostructures (HM/FM/I). Employing *ab initio* electronic structure calculations we have investigated the effect of epitaxial strain and thickness of both FeCo and Ir layers as design parameters to optimize the PMA and VCMA of Ir/FeCo/MgO. We predict that the Ir cap layer can induce both large PMA and colossal VCMA efficiency which depend on the stain. More importantly, we predict that a single Ir cap monolayer gives rise to a VCMA efficiency one order of magnitude higher than that of thicker Ir layers. The underlying mechanism is the synergistic effects of the emergence of Ir local moments, the large Ir spin orbit coupling (SOC), and the large modulation of the magnetic anisotropy at the Ir/vacuum interface. These results provide useful guiding rules in the design of the next-generation of high performance MeRAM memory devices.

PACS numbers: 75.85.+t, 73.20.-r, 75.30.Gw, 75.70.Cn

I. INTRODUCTION

In the development process of memory technologies, memory devices have evolved progressively focusing on their size and performance attributes. To mitigate the disadvantages of current memory devices, there is an urgent need in developing the next-generation of nonvolatile, high-speed, low-power consumption and high area-density memories. In this vein, magnetic random access memory (MRAM) has emerged as a promising alternative to the widely used complementary metal-oxide semiconductor (CMOS) based memory devices, where spin transfer torque (STT)[1,2] or spin-orbit torque (SOT)[3–6] mechanisms of magnetization switching have been employed for the reading/writing of information. Although MRAM has proven successful[7], it still requires large dynamic power for magnetization switching and high current densities which in turn result in Joule heating.

Magnetoelectric random access memory (MeRAM) is an emerging memory device technology which paves the way for ultra-low power, highly-scalable, and non-volatile spin-based RAMs.[8] MeRAM utilizes the so-called voltage-controlled magnetic anisotropy (VCMA) mechanism, where the energy barrier between the two states of magnetization can be tuned under an external electric field (E_{ext}) applied across a heavy-metal/ferromagnet/insulator (HM/FM/I) heterostructure. In the linear regime, the VCMA=$\beta E_I = \beta E_{ext}/\epsilon_\perp$, where β is the VCMA efficiency, E_I is the electric field inside the insulator, and $\epsilon_\perp$ is the out-of-plane component

of the relative dielectric constant tensor of the insulator which depends on strain and the type of the insulator[9,10]. MeRAM surpasses the limit of STT-RAM and the previous memory devices. For example, the switching energy per bit of MeRAM ($\sim$1 fJ) is lower than that in static random access memory (SRAM) and STT-RAM ($\sim$100 fJ) and has a comparable write and read access speed (1-10 ns).[11,12] It also provides a higher areal density similar to DRAM, and promises a higher endurance than other memory devices.[13]

To date there are two major bottlenecks in optimizing the performance of MeRAM devices: (1) Large perpendicular magnetic anisotropy (PMA) (higher than 2 erg/cm^2) to ensure the stability of the magnetic bit at room temperature; and (2) High VCMA efficiency ($\beta \geq 1,000$ fJ/Vm) in order to replace DRAM at 7 nm node.[14,15] In recent years intense experimental[8,11,12,15–17] and theoretical[9,10,18–23] efforts have focused on understanding the possible mechanisms that govern the VCMA and identifying materials to achieve both high PMA and VCMA efficiency. Nevertheless, experimental works in Ta/$Co_{40}Fe_{40}B_{20}$/MgO[16,24], Au/FeCo/MgO[25], and Ir-doped Fe/MgO[26] have reported overall rather limited values of PMA ($<$ 2 erg/cm^2) and VCMA (100-300 fJ/Vm) efficiency. Interestingly, recent experiments using crystallographically *strained* CoFe layer in MgO/FeCo/Ir heterostructures[27] have reported record-high VCMA coefficient exceeding 1,000 fJ/(Vm).

The objective of this manuscript is to employ first principles electronic structure calculations to investigate the effect of epitaxial strain on the magnetic anisotropy (MA)
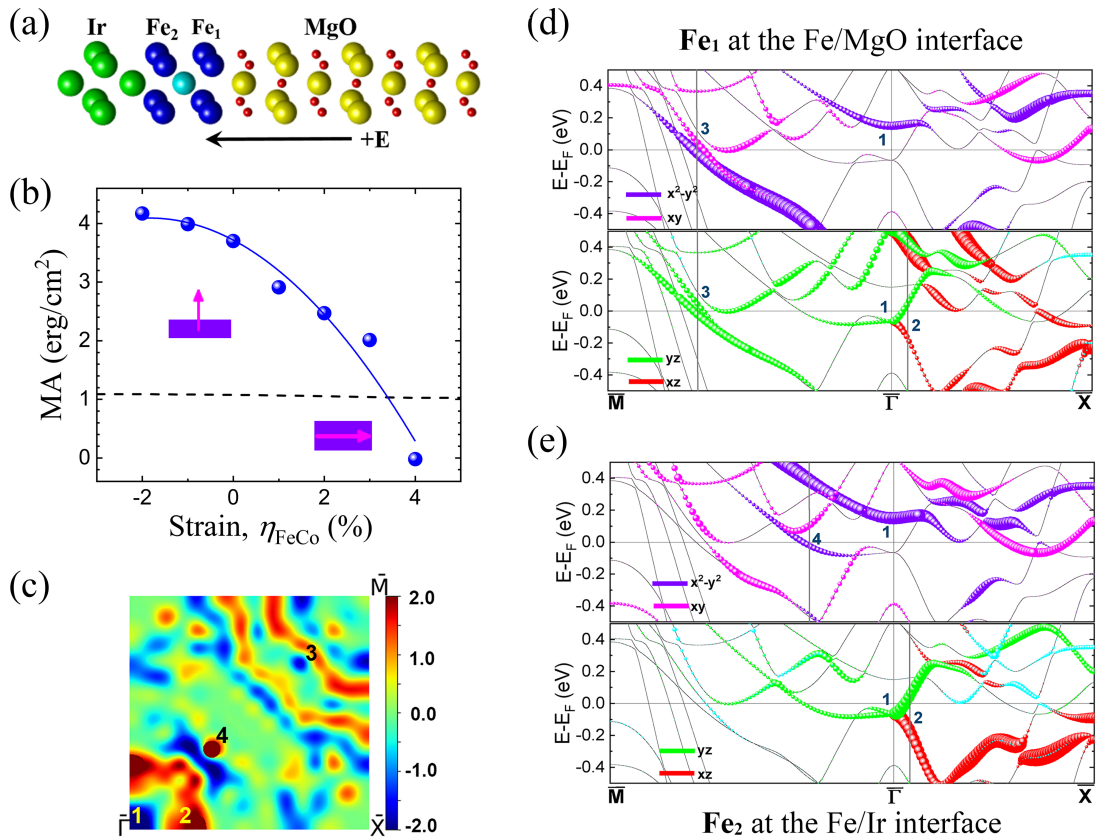
FIG. 1: (a) Ir(3)/FeCo(3)/MgO(7) slab supercell, where the integers in the parentheses refer to the number of monolayers. Also we show the positive direction of the external electric field. (b) Strain dependence of zero-field MA where closed circles denote the *ab initio* results and the curve is a quadratic fit. The horizontal line denotes the shape anisotropy energy, $|K^s|$, of the slab which is relatively strain independent. (c) **k**-resolved MA (in erg/cm^2) in the 2D BZ for η_{FeCo}=0%. Energy- and **k**-resolved distributions of the *d*-orbital character of minority-spin bands along symmetry directions for (d) Fe$_1$ (at the Fe/MgO interface) and (e) Fe$_2$ (at the Fe/Ir interface). Numerals in (c)-(e) refer to BZ $\mathbf{k}_\parallel$ points (BZPn, n=1-4) where the MA has large positive or negative contributions.

and the VCMA in Ir/FeCo/MgO heterostructures. We predict that the Ir overlayer yields colossal electric field modulation of the magnetic anisotropy which depends on the epitaxial strain, the FeCo- and Ir-thickness. More specifically, we demonstrate that the single monolayer Ir overlayer yields giant VCMA coefficient exceeding 13,000 fJ/(Vm). Detailed analyses of the spin- and the atom-resolved decompositions of the MA elucidate the underlying origin of the giant electric field control of the magnetic anisotropy and provide design guidelines for future experiments to optimize the VCMA efficiency.

The rest of this paper is organized as follows: Sec. II describes the methodology used to calculate the MA. In Sec. IIIA, we present results of the effect of strain on the zero-field magnetic anisotropy. The effect of the FeCo thickness on the magnetic anisotropy is discussed in Sec. IIIB. In Sec. IIIC, we present results of the effect of Ir thickness on the magnetic properties of the Ir(n)/FeCo/MgO heterostructure and show that a sin-

gle Ir cap layer leads to a giant VCMA coefficient. In Sec. IIID, we present results of the effect of strain on the VCMA behavior and elucidate the underlying origin. Finally, conclusions are summarized in Sec. IV.

II. COMPUTATIONAL METHODS AND MODELS

The *ab initio* calculations have been carried out within the framework of the projector augmented-wave formalism[28] as implemented in the Vienna *Ab initio* Simulation Package (VASP)[29] with the Perdew-Burke-Ernzerhof functional form of the generalized gradient approximation for the exchange-correlation interaction.[30] We employ the slab supercell approach along [001] consisting of of fcc Ir and *B*2-type FeCo layers of variable thicknesses and seven monolayers (MLs) of rock-salt MgO. The periodic slabs are separated by a 15-Å-thick vacuum. We

build up supercells by aligning the $\langle 110 \rangle$ axis of MgO and Ir with the $\langle 100 \rangle$ axis of FeCo as shown in Fig. 1 (a). The FeCo/MgO interface is designed by placing the O atoms atop the Fe atoms. Fe_1 and Fe_2 denote the iron atoms at the Fe/MgO and Fe/Ir interfaces, respectively.

The experimental values of the MgO and FeCo lattice constants[31] of 2.978 Å and 2.850 Å respectively, result in a large tensile strain of $\sim 4.49\%$ on the FeCo layer assuming that the MgO substrate is unstrained. In order to investigate the effect of strain on the MA of the system, we have varied η_{FeCo} from -2%, corresponding to the unstrained Ir lattice constant, to $+4\%$, nearly unstrained MgO lattice constant. Here, the strain is defined as, $\eta_{FeCo} = (a_{FeCo} - a_{FeCo}^{(0)})/a_{FeCo}^{(0)}$, where $a_{FeCo}^{(0)} = 2.8417$ Å is the calculated equilibrium lattice constant of bulk FeCo. At each strain, the magnetic, electronic degrees of freedom and atomic z positions are fully optimized until forces acting on the ions become less than 5×10^{-3} eV/Å and the change in the total energy between two ionic relaxation steps is smaller than 10^{-6} eV.

Employing $16 \times 16 \times 1$ k-grid for the relaxations and $32 \times 32 \times 1$ k-grid for the spin-orbit-coupling (SOC) calculations, the MA per unit area can be determined from $MA = (E_{[100]} - E_{[001]})/A$, where $E_{[100]}$ and $E_{[001]}$ are total energies with the magnetization along the [100] and [001] directions, respectively, and A is the in-plane area of the unit cell. We use a cut-off energy of 500 eV and apply dipole corrections along the z-axis. For the electric field calculations, an electric field is applied along the [001] direction and the atomic z positions, and magnetic and electronic degrees of freedom are optimized at each electric field.

III. RESULTS AND DISCUSSION

A. Effect of Strain on Zero-Field Magnetic Anisotropy

Fig. 1(b) displays the variation of the zero-field MA with biaxial strain, η_{FeCo}, for the Ir(3)/FeCo(3)/MgO(7) heterostructure, where the numbers in the parenthesis denote MLs. The dashed line denotes the shape anisotropy energy, $K^s = -\frac{1}{2}\mu_o M_s^2 t = -1.01$ erg/cm^2, of the slab which is relatively strain independent. Here, M_s is the magnetic moment per unit volume and t is the thickness of the FeCo thin film. The calculated saturation magnetization, $M_s = 1846$ emu/cm^3, is in good agreement with the experimental value[27] of 1954 emu/cm^3. The effective magnetic anisotropy $K_{eff}t = MA + K^s$. The dashed curve denotes the quadratic fit to the *ab initio* calculated MA values. Note that, for a wide range of strain (-2 to +3%), the Ir(3)/FeCo(3)/MgO(7) system exhibits large PMA ($\approx +2$ to $+4$ erg/cm^2) which is about twice as large as those of Ta[9] and Au[10] capped systems indicating that the Ir cap enhances the PMA. Note that the system undergoes a spin reorientation tran-
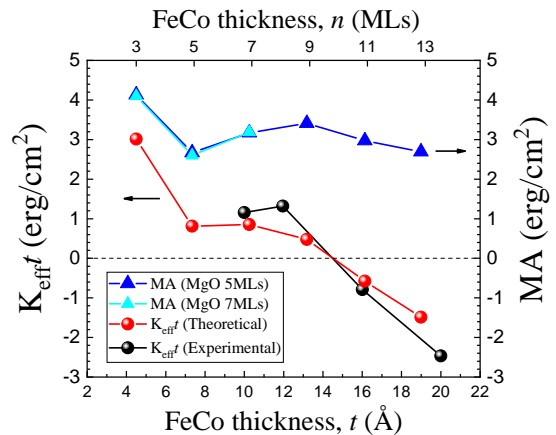
FIG. 2: Variation of the *ab initio* magnetic anisotropy, MA (triagles), effective magnetic anistropy, $K_{eff}t$ (circles) with the FeCo thickness, t, for the Ir(3)/FeCo(n)/MgO(7) heterostructure, where the numbers in the parentheses denote the number of monolayers. For comparison, we also show the experimental results (black circles)[27].

sition to an in-plane magnetization orientation at about 3.5% strain.

In order to understand the underlying mechanism of the strain-induced MA, in Fig. 1(c) we show the $\mathbf{k}$-resolved MA, $MA(\mathbf{k}) = \sum_{n \in occ}[\epsilon(n,\mathbf{k})^{[100]} - \epsilon(n,\mathbf{k})^{[001]}]$, in the two-dimensional (2D) Brillouin zone (BZ) calculated using the force theorem[32]. Here, $\epsilon(n,\mathbf{k})^{[100]}$ represents the eigenvalues of the Hamiltonian for magnetization along the [100] axis. Using the tetrahedron method with Blöchl corrections[33], the MA values calculated from the force theorem are in very good agreement with those obtained from total energy calculations for all strains.

Fig. 1(d) and (e) show the energy- and $\mathbf{k}$-resolved distributions of the d-orbital characters of the minority-spin bands for the Fe_1 (at the Fe/MgO interface) and Fe_2 (at the Fe/Ir interface) atoms along the high symmetry lines in the 2D BZ for $\eta_{FeCo}=0$ %. Within second-order perturbation theory the MA can be expressed as[34]

$$MA \approx \sum_{o,u} \frac{|\langle \Psi_o^{\downarrow}|\hat{\xi}\hat{L}_z|\Psi_u^{\downarrow}\rangle|^2 - |\langle \Psi_o^{\downarrow}|\hat{\xi}\hat{L}_x|\Psi_u^{\downarrow}\rangle|^2}{E_u^{\downarrow} - E_o^{\downarrow}}$$
$$+ \sum_{o,u} \frac{|\langle \Psi_o^{\uparrow}|\hat{\xi}\hat{L}_x|\Psi_u^{\downarrow}\rangle|^2 - |\langle \Psi_o^{\uparrow}|\hat{\xi}\hat{L}_z|\Psi_u^{\downarrow}\rangle|^2}{E_u^{\downarrow} - E_o^{\uparrow}}, \quad (1)$$

where $\Psi_o^{\downarrow}(E_o^{\downarrow})$, $\Psi_o^{\uparrow}(E_o^{\uparrow})$, and $\Psi_u^{\downarrow}(E_u^{\downarrow})$ are occupied minority-spin, occupied majority-spin, and unoccupied minority-spin states (energies) of band index n and wave vector $\mathbf{k}$, $\hat{\xi}$ is a diagonal matrix whose matrix elements are the atomic SOC constants, and $\hat{L}_{z(x)}$ is out-of (in) plane components of the orbital angular momentum operator.

At zero strain, the negative MA($\mathbf{k}_{\parallel}$) at $\overline{\Gamma}$ (BZP1) in Fig. 1(c) arises from the SOC of the minority-spin occupied $d_{xz}(d_{yz})$ states with the unoccupied $d_{x^2-y^2}$ states of
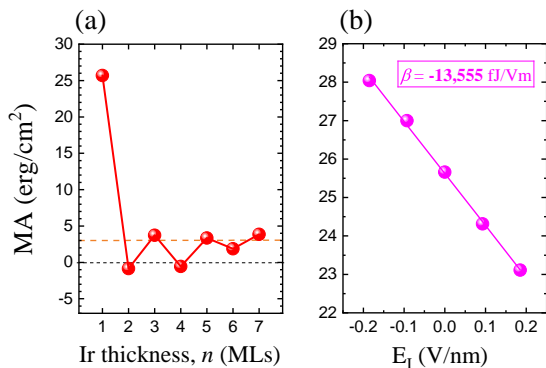
FIG. 3: (a) MA versus Ir cap thickness. (b) MA versus electric field in insulator for the system with a single Ir ML.

TABLE I: Values of the layer-resolved Ir magnetic moment (in μ_B) for different Ir thickness (in ML) for the Ir(n)/FeCo(3)/MgO(7) heterostructure under η_{FeCo}=0% (or $a_{FeCo} = 2.8417$ Å). The Ir$_1$ layer refers to the Ir atom at the Ir/FeCo interface.

Ir thickness (ML)	μ_{Ir_1}	μ_{Ir_2}	μ_{Ir_3}	μ_{Ir_4}
1	0.81	-	-	-
2	0.20	-0.51	-	-
3	0.26	-0.07	0.03	-
4	0.27	-0.10	-0.02	0.05

both Fe$_1$ and Fe$_2$ interfacial atoms in Fig. 1(d) and (e), through the in-plane orbital angular momentum operator $\hat{L}_x$. On the other hand, the large positive MA($\mathbf{k}_\parallel$) at BZP2 along $\overline{\Gamma X}$ arises from the SOC $\langle xz(yz)|\hat{L}_z|yz(xz)\rangle$ of the minority-spin states of both interfacial Fe$_1$ and Fe$_2$ atoms. Similarly, the positive MA($\mathbf{k}_\parallel$) at BZP3 along the $\overline{M\Gamma}$ direction is due to the SOC $\langle d_{x^2-y^2}|\hat{L}_z|xy\rangle$ and $\langle xz(yz)|\hat{L}_z|yz(xz)\rangle$ minority-spin Fe$_1$-derived states, while the positive MA at BZP4 originates from the SOC between minority-spin Fe$_2$-derived occupied $d_{x^2-y^2}$ states and the unoccupied d_{xy} states via the out-of-plane operator $\hat{L}_z$. It is important to emphasize that in contrast to our previous calculations of the Ta[9] and Au[10] cap where only the Fe$_1$ atom at the Fe/MgO interface was giving the dominant contribution to the MA, for the Ir overlayer both interfacial Fe$_1$ and Fe$_2$ yield similar contributions.

B. Effect of FeCo Thickness on Magnetic Anisotropy

Fig. 2 shows the variation of MA with FeCo thickness in the Ir(3 ML)/FeCo (n ML)/MgO(5 ML) trilayer under -2% compressive biaxial strain on the FeCo[27]. Calculations employing seven MgO MLs for thinner FeCo ($\leq$ 7 ML) films (also shown in Fig. 2) demonstrate that the 5 ML-thick MgO is sufficient to obtain accurate values of MA. The MA exhibits a damped oscillatory behavior with the FeCo thickness which eventually saturates at $\approx$ 2.8 erg/cm^2 for thicker FeCo. This typical oscillatory behavior is due to the interplay of negative and positive MA contributions from SOC of various quantum well states around the Fermi level, whose number and energy positions depend on the FM thickness.[35,36]

Analysis of $\mathbf{k}$-resolved MA shows : (i) The large MA for 3 MLs arises from the SOC $\langle d_{x^2-y^2}|\hat{L}_z|d_{xy}\rangle$ and $\langle d_{xz(yz)}|\hat{L}_z|d_{yz(xz)}\rangle$ minority-spin Fe$_2$-derived states; (ii) For the 5 ML the unoccupied minority-spin d_{z^2}-derived states of Fe$_2$ emerge at the Fermi level which in turn

couple with the occupied d_{xz} via the in-plane angular momentum operator, $\hat{L}_x$, yielding a negative contribution to the MA. Moreover, the energy separation between the occupied $d_{x^2-y^2}$ and unoccupied d_{xy} states increases, reducing further the MA. These two effects result in a decrease of the PMA from 4.17 to 2.6 erg/cm^2; (iii) For the 7 ML thickness of FeCo the increase of the PMA is due to the reappearance of SOC between unoccupied $d_{x^2-y^2}$ and occupied d_{xy} derived-states of the interfacial Fe$_2$. In order to compare with recent experiments[27] we have also calculated the effective MA, $K_{eff}t$, as a function of the FeCo thickness which is shown also in Fig. 2, where the agreement is good. Note that $K_{eff}t$ becomes negative for FeCo thickness beyond 1.5 nm ($\sim$10 ML), indicating a spin reorientation from out-of to in-plane magnetization orientation. For $t > 1.5$ nm $K_{eff}t$ varies linearly with thickness due to the fact that the MA saturates almost to a constant value and the shape anisotropy energy decreases linearly with the FeCo thickness.

C. Effect of Ir Thickness on Magnetic Anisotropy

We have also investigated the effect of Ir thickness on the magnetic properties of the Ir(n)/FeCo(3 ML)/MgO(7 ML) heterostructure under η_{FeCo}=0%, where n= 1-7 MLs. The variation of the MA as a function of the thickness of the Ir overlayer is shown in Fig. 3(a). We find a colossal MA value of 26 erg/cm^2 for a single Ir monolayer in agreement with previous calculations for the Fe/Ir bilayer[37]. The underlying origin is the spin-flip SOC between occupied majority-spin d_{yz}-derived states and unoccupied of minority-spin d_{z^2}-derived states of the *interfacial Ir* (Ir$_1$ in Table I) at the Ir/FeCo interface. Interestingly, the interfacial Ir atom (at the Ir/FeCo interface) does not contribute significantly when the Ir thickness larger than 1 ML. The MA shows an oscillatory behavior from 2 to 7 ML Ir exhibiting peaks and troughs at odd and even numbers of Ir MLs, respectively. Analysis of the energy- and $\mathbf{k}$-resolved distributions of Fe$_1$ and Fe$_2$ d-states shows that the oscillation is induced by the SOCs between the minority-spin $d_{x^2-y^2}$- and d_{xy}- derived states of the Fe$_2$ interfacial atom which consistently occurs and vanish at odd and even numbers of Ir MLs, respectively.
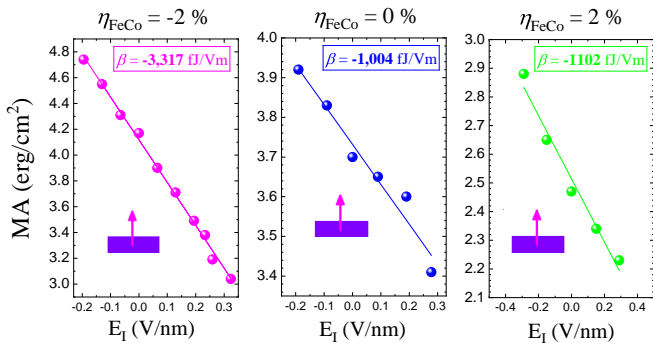
FIG. 4: MA as a function of electric field in MgO for the Ir(3)/FeCo(3)/MgO(7) heterostructure under different strain values, $\eta_{FeCo} = -2$, 0, and 2%. Insets: Schematic out-of-plane magnetization orientation for the thin film.

FIG. 5: (a) Minority-spin band structure of Ir(3)/FeCo(3)/MgO(7) for $\eta_{FeCo} = -2\%$ under $E_I = 0$ (dotted black curves), -0.13 V/nm (solid green curves), and $+0.33$ V/nm (solid pink curves). Electric field induced change of MA, $\Delta MA(\mathbf{k})$, (in erg/cm^2) in the two-dimensional Brillouin zone under (b) $E_I = -0.13$ and (c) $+0.33$ V/nm, respectively.

Table I lists the layer-resolved magnetic moments of the Ir overlayer for different Ir thickness for $\eta_{FeCo} = 0\%$. We find a local moment of $0.81\mu_B$ for a single Ir(1 ML)/FeCo in agreement with previous calculations[37] for the Ir/Fe bilayer. For $n \geq 2$ the interfacial Ir local moment remains constant around 0.26 μ_B. Note that the local moment for a free standing Ir ML under $\eta_{FeCo} = 0\%$ is about 1.65 μ_B and decreases to about 0.5 μ_B at about 2.715 Å(bulk lattice constant of Ir). The hybridization of the Fe d states with those of Ir results in a reduction of the local Ir moment from its free-standing value by a factor of two. Thus, the emergence of the giant PMA for the Ir(1 ML)/FeCo arises from the rather large local Ir moment due to the *tensile* biaxial strain ($\sim +4\%$) the Ir ML experiences. This is in sharp contrast to the low interfacial local moments of Ta[9] and Au[10] caps both of which are under large *compressive* biaxial strain.

The synergistic effects of (i) the local magnetic moment of the Ir ML, (ii) the large SOC constant of Ir (~ 0.45 eV), and (iii) the presence of E_{ext} at the vacuum/Ir interface invites the intriguing question whether the Ir monolayer cap exhibits also a giant VCMA effect. Fig. 3(b) shows the MA as a function of electric field in MgO for the Ir(1)/FeCo(3)/MgO(7) slab under $\eta_{FeCo}=0$. We predict a colossal VCMA coefficient, $|\beta| = 13{,}555$ fJV^{-1}m^{-1}. Analysis of the energy- and k-resolved distribution of d-states reveals that SOCs of the *Ir* atoms give the dominant contribution to the VCMA due to its large SOC. The increase (decrease) of the MA under negative (positive) E_{ext} is due to the increase (decrease) of the energy separation (denominator in Eq. (1)) between the interfacial Ir-derived occupied majority-spin d_{yz} states coupled with the minority-spin Ir d_{xz} states which are coupled through $\hat{L}_z$.

D. Effect of strain on VCMA of Ir/FeCo/MgO

Fig. 4 shows the variation of the MA as a function of electric field in the MgO layer (E_I) for the Ir(3)/FeCo(3)/MgO(7) heterostructure under different values of biaxial strain. We have found that the relative dielectric constant, $\varepsilon_\perp/\varepsilon_0$, increases exponentially with increasing compressive strain on the insulator (i.e., decreasing expansive strain on the FM). The calculated values of $\varepsilon_\perp/\varepsilon_0$ are 10.7, 17.0, 27.0, and 38.6 for $\eta_{FeCo} = 4$, 2, 0, and -2 %, respectively.[9,10] The results reveal linear VCMA behavior with giant VCMA coefficients, $|\beta| = 3{,}317$, 1,004, and 1,102 fJV^{-1}m^{-1} for $\eta_{FeCo} = -2$, 0, and 2 %, respectively. A compressive strain of about -2% is most likely induced in the recent experiments[27] in Ir/FeCo/MgO junctions with relatively thick Ir caps. Overall, these values of VCMA coefficient are much higher than those we reported for Ta- and Au-based caps.

In order to understand the VCMA behavior under -2% strain (as a representative example), in Fig. 5(a) we show the shifts of the minority-spin energy bands under electric fields $E_I^- = -0.13$ V/nm (solid green curves) and $E_I^+ = +0.33$ V/nm (solid pink curves) relative to the zero-field bands (dashed black curves). Fig. 5(b) and (c) show the field-induced MA change, $\Delta MA(\mathbf{k}) = MA(\mathbf{k},E) - MA(\mathbf{k},E=0)$ in the 2D BZ under

-0.13 and +0.33 V/nm, respectively. One of the obvious changes occurs at BZP1 ($\frac{1}{3}\overline{\Gamma M}$) where MA($\mathbf{k}$) reverses sign when E_I changes from -0.13 to +0.33 V/nm. Analysis of the atom- and orbital-resolved band structure at BZP1 shows that the only significant SOC is between spin-minority occupied $d_{x^2-y^2}$ and unoccupied d_{xy} derived states of the Fe$_2$ interfacial atom coupled through $\hat{L}_z$, which in turn yields positive MA contribution. We find that under the negative (positive) field, the energy separation between these two states is decreased (increased) by -4 meV ($+7$ meV), leading to the positive (negative) ΔMA($\mathbf{k}$) at BZP1.

3,317 to 1,004 fJV^{-1}m^{-1}, due to magnetoelectrically active Ir/FeCo interface. The origin of the predicted giant VCMA coefficient of 13,555 fJV^{-1}m^{-1} for the single Ir ML capped system arises from the synergistic effects of (i) the local magnetic moment of the Ir ML; (ii) the large SOC of Ir; and (iii) the presence of E_{ext} at the vacuum/Ir interface. A single Ir monolayer cap can be realized using atomic layer deposition or pulsed layer deposition techniques. These calculations provide useful guiding rules in the design of the next-generation Ir-based MeRAM devices to achieve low energy dissipation up to two orders of magnitude.

IV. CONCLUSIONS

Employing *ab initio* electronic structure calculations, we have investigated the effect of epitaxial strain, FeCo thickness, and Ir cap thickness, as design parameters to optimize the PMA and VCMA of Ir/FeCo/MgO heterostructures. We have demonstrated that the Ir-capped systems have giant VCMA coefficients in the range of

Acknowledgments

---

* Electronic address: sohee.kwon.866@my.csun.edu

† Electronic address: nick.kioussis@csun.edu

[1] J. C. Slonczewski, Current-driven excitation of magnetic multilayers, J. Magn. Magn. Mater. **159**, L1-L7 (1996).

[2] L. Berger, Emission of spin waves by a magnetic multilayer traversed by a current, Phys. Rev. B **54**, 9353 (1996).

[3] I. M. Miron, K. Garello, G. Gaudin, P. J. Zermatten, M. V. Costache, S. Auffret, S. Bandiera, B. Rodmacq, A. Schuhl and P. Gambardella, Perpendicular switching of a single ferromagnetic layer induced by in-plane current injection, Nature **476**, 189193 (2011).

[4] L. Liu, O. J. Lee, T. J. Gudmundsen, D. C. Ralph, and R. A. Buhrman, Current-Induced Switching of Perpendicularly Magnetized Magnetic Layers Using Spin Torque from the Spin Hall Effect, Phys. Rev. Lett. **109**, 096602 (2012).

[5] L. Liu, C. F. Pai, Y. Li, H. W. Tseng, D. C. Ralph, and R. A. Buhrman, Spin-Torque Switching with the Giant Spin Hall Effect of Tantalum, Science **336**, 555 (2012).

[6] I. M. Miron, G. Gaudin, S. Auffret, B. Rodmacq, A. Schuhl, St. Pizzini, J. Vogel and P. Gambardella, Current-driven spin torque induced by the Rashba effect in a ferromagnetic metal layer, Nature Mater. **9**, 230234 (2010).

[7] C. Chappert, A. Fert, and F. N. Van Dau, The emergence of spin electronics in data storage, Nature Mater. **6**, 813 (2007).

[8] Y. Shiota, T. Nozaki, F. Bonell, S. Murakami, T. Shinjo, and Y. Suzuki, Induction of coherent magnetization switching in a few atomic layers of FeCo using voltage pulses, Nature Mater. **11**, 39 (2012).

[9] P. V. Ong, N. Kioussis, D. Odkhuu, P. K. Amiri, K. L. Wang, and G. P. Carman, Giant voltage modulation of magnetic anisotropy in strained heavy metal/magnet/insulator heterostructures. Phys. Rev. B **92**, 020407(R) (2015).

[10] P. V. Ong, N. Kioussis, P. K. Amiri and K. L. Wang, Electric-field-driven magnetization switching and nonlinear magnetoelasticity in Au/FeCo/MgO heterostructures. Sci. Rep. **6**, 29815 (2016).

[11] C. Grezes, F. Ebrahimi, J. G. Alzate, X. Cai, J. A. Katine, J. Langer, B. Ocker, P. K. Amiri, and K. L. Wang, Ultra-low switching energy and scaling in electric-field-controlled nanoscale magnetic tunnel junctions with high resistance-area product, Appl. Phys. Lett. **108** (1), 012403 (2016).

[12] Y. Shiota, T. Nozaki, S. Tamaru, K. Yakushiji, H. Kubota, A. Fukushima, S. Yuasa, Y. Suzuki, Reduction in write error rate of voltage-driven dynamic magnetization switching by improving thermal stability factor, Appl. Phys. Lett. **111**, (2017).

[13] R. Dorrance, J. G. Alzate, S. S. Cherepov, P. Upadhyaya, I. N. Krivorotov, J. A. Katine, J. Langer, K. L. Wang, P. K. Amiri, and D. Markovic, Diode-MTJ Crossbar Memory Cell Using Voltage-Induced Unipolar Switching for High-Density MRAM, IEEE Electron Device Lett. **34** (6), 753 (2013).

[14] X. Li, Interface Engineering of Voltage-Controlled Embedded Magnetic Random Access Memory, PhD dissertation, University California Los Angeles, Retrieved from https://escholarship.org/uc/item/2t0089x7 (2018)

[15] K. L. Wang, J. G. Alzate and P. K. Amiri, Low-power non-volatile spintronic memory: STT-RAM and beyond, J. Phys. D: Appl. Phys. **46** 074003 (2013)

[16] W.-G. Wang, M. Li, S. Hageman, and C. L. Chien, Electric-field-assisted switching in magnetic tunnel junctions, Nature Mater. **11**, 64 (2012).

[17] T. Nozaki, A. Kozio-Rachwa, W. Skowroski, V. Zayets, Y. Shiota, S. Tamaru, H. Kubota, A. Fukushima, S. Yuasa, and Y. Suzuki, Large Voltage-Induced Changes in the Perpendicular Magnetic Anisotropy of an MgO-Based Tunnel Junction with an Ultrathin Fe Layer, Phys. Rev. Applied **5**, 044006 (2016).

[18] K. Nakamura, R. Shimabukuro, Y. Fujiwara, T. Akiyama, T. Ito, and A. J. Freeman, Giant Modification of the Magnetocrystalline Anisotropy in Transition-Metal Monolayers by an External Electric Field, Phys. Rev. Lett. **102**, 187201 (2009).

[19] C.-G. Duan, J. P. Velev, R. F. Sabirianov, Z. Zhu, J. Chu, S. S. Jaswal, and E. Y. Tsymbal, Surface Magnetoelectric Effect in Ferromagnetic Metal Films, Phys. Rev. Lett. **101**, 137201 (2008).

[20] M. K. Niranjan, C.-G. Duan, S. S. Jaswal, and E. Y. Tsymbal, Electric field effect on magnetization at the Fe/MgO(001) interface, Appl. Phys. Lett. **96**, 222504 (2010)

[21] P. V. Ong, N. Kioussis, P. K. Amiri, J. G Alzate, K. L. Wang, G. P. Carman, J. Hu, and R. Wu, Electric field control and effect of Pd capping on magnetocrystalline anisotropy in FePd thin films: A first-principles study, Phys. Rev. B **89**, 094422 (2014).

[22] J. Zhang, P. V. Lukashev, S. S. Jaswal, and E. Y. Tsymbal, Model of orbital populations for voltage-controlled magnetic anisotropy in transition-metal thin films, Phys. Rev. B **96**, 014435 (2017).

[23] K. Nakamura, T. Nomura, A. M. Pradipto, K. Nawa, T. Akiyama, T. Ito, Effect of heavy-metal insertions at Fe/MgO interfaces on electric-field-induced modification of magnetocrystalline anisotropy, J. Magn. Magn. Mater. **429**, 214-220 (2017).

[24] M. Endo, S. Kanai, S. Ikeda, F. Matsukura, and H. Ohno, Electric-field effects on thickness dependent magnetic anisotropy of sputtered $MgO/Co_{40}Fe_{40}B_{20}/Ta$ structures, Appl. Phys. Lett. **96**, 212503 (2010).

[25] T. Nozaki, Y. Shiota, M. Shiraishi, T. Shinjo, and Y. Suzuki, Voltage-induced perpendicular magnetic anisotropy change in magnetic tunnel junctions, Appl. Phys. Lett. **96**, 022506 (2010).

[26] T. Nozaki, A. Kozio-Rachwa, M. Tsujikawa, Y. Shiota, X. Xu, T. Ohkubo, T. Tsukahara, S. Miwa, M. Suzuki, S. Tamaru, H. Kubota, A. Fukushima, K. Hono, M. Shirai, Y. Suzuki and S. Yuasa, Highly efficient voltage control of spin and enhanced interfacial perpendicular magnetic anisotropy in iridium-doped Fe/MgO magnetic tunnel junctions, NPG Asia Mater. **9**, e451 (2017).

[27] Y. Kato, H. Yoda, Y. Saito, S. Oikawa, K. Fujii, M. Yoshiki, K. Koi, H. Sugiyama, M. Ishikawa, T. Inokuchi, N. Shimomura, M. Shimizu, S. Shirotori, B. Altansargai, Y. Ohsawa, K. Ikegami, A. Tiwari and A. Kurobe, Giant voltage-controlled magnetic anisotropy effect in a crystallographically strained CoFe system, Appl. Phys. Express **11**, 053007 (2018).

[28] P. E. Blchl, Projector augmented-wave method, Phys. Rev. B **50**, 17953 (1994).

[29] G. Kresse and J. Furthmller, Efficient iterative schemes for ab initio total-energy calculations using a plane-wave basis set, Phys. Rev. B **54**, 11169 (1996).

[30] J. P. Perdew, K. Burke, and M. Ernzerhof, Generalized Gradient Approximation Made Simple, Phys. Rev. Lett. **77**, 3865 (1996)

[31] P. Villars, L. D. Calvert, Pearsons Handbook of Crystallographic Data for Intermetallic Phases, ASM International, Materials Park, OH (1991).

[32] M. Weinert, R. E. Watson, and J. W. Davenport, Total-energy differences and eigenvalue sums, Phys. Rev. B **32**, 2115 (1985).

[33] P. E. Blchl, O. Jepsen and O. K. Andersen, Improved tetrahedron method far Brilleuin-zane integratians, Phys. Rev. B **49**, 16223 (1994).

[34] D.-S. Wang, R. Wu, and A. J. Freeman, First-principles theory of surface magnetocrystalline anisotropy and the diatomic-pair model. Phys. Rev. B **47**, 14932 (1993).

[35] C. H. Back, W. Weber, Ch. Wrsch, A. Bischof, D. Pescia and R. Allenspach, Magnetic anisotropy oscillations, J. Appl. Phys. **81**, 5054 (1998).

[36] P. V. Ong, N. Kioussis, P. K. Amiri and K. L. Wang, Oscillatory magnetic anisotropy and spin-reorientation induced by heavy-metal cap in Cu/FeCo/M (M = Hf or Ta): A first-principles study Phys. Rev. B **94**, 174404 (2016)

[37] D. Odkhuu, S. H. Rhim, N. Park, and S. C. Hong, Extremely large perpendicular magnetic anisotropy of an Fe(001) surface capped by 5d transition metal monolayers: A density functional study, Phys. Rev. B **88**, 184405 (2013).